

Modal Analysis of Water Distribution Systems with the Elastic Water Column Model

Morteza Imani¹, Wei Zeng², Aaron Zecchin³, Martin F. Lambert⁴

⁴ ¹PhD Candidate; School of Architecture and Civil Engineering, University of Adelaide, SA
⁵ 5005, Australia; Email: morteza.imani@adelaide.edu.au

6 ²Lecturer; School of Architecture and Civil Engineering, University of Adelaide, SA 5005,
7 Australia; Email: w.zeng@adelaide.edu.au

³Senior Lecturer; School of Architecture and Civil Engineering, University of Adelaide, SA 5005, Australia; Email: aaron.zecchin@adelaide.edu.au

10 ⁴Professor; School of Architecture and Civil Engineering, University of Adelaide, SA 5005,
11 Australia; Email: martin.lambert@adelaide.edu.au

12 Abstract

This paper presents a modal and participation factor (PF) analysis of water distribution systems (WDSs) using the elastic water column model (EWCM). Modal analysis, widely used in other engineering fields, is adapted here to characterize the dynamic behavior of WDSs under transient conditions. By linearizing the EWCM around an operating point, a state-space representation is developed, enabling the extraction of natural modes via eigenvalue analysis. These modes, defined by their frequencies and damping ratios, are validated through comparison with the admittance matrix method (AMM) in the frequency domain. The study introduces PF analysis to quantify how each state variable (nodal head or flow rate) contributes

21 to each mode. This spatial information identifies critical locations that are more sensitive to
22 excitations and capable of amplifying transient responses. To verify the effectiveness of PF
23 analysis, time-domain simulations are conducted for three test cases, including a real-world
24 network (the New York tunnel system). The results confirm that exciting the system at high-
25 PF locations can generate significant transients, while low-PF locations produce minimal
26 responses. The analysis also reveals how resonance behavior in WDSs is spatially distributed,
27 enabling the identification of vulnerable areas where transients are amplified. This work
28 provides a unified time-domain framework for modal and PF analysis, contributing to
29 improved system monitoring, management, and fault detection in WDSs.

30 **Keywords:** Elastic water column model; Modal analysis; Participation factor; Hydraulic
31 transient.

32 **Introduction**

33 Modal analysis is a widely used engineering technique for determining the dynamic
34 characteristics of systems by identifying their natural frequencies, damping ratios, and mode
35 shapes. It is particularly valuable in fields such as mechanical and civil engineering, where it
36 helps predict how structures will respond to external forces, ensuring stability and identifying
37 potential vulnerabilities. Modal analysis also plays a key role in the study of inter-area
38 oscillations in power grids, helping to understand electro-mechanical oscillations ([Dussaud, 2015](#);
39 [Klein et al., 1991](#)). Furthermore, it has been extensively applied in aerospace, automotive
40 design, and earthquake engineering, where understanding system dynamics is essential for both
41 performance and safety ([Dussaud, 2015](#); [He & Fu, 2001](#)).

42 Despite its broad use in other engineering disciplines, the application of modal analysis to
43 WDSs remains limited. WDSs are subject to hydraulic transients caused by sudden changes in
44 demand, pump failures, or valve operations. These transients can generate pressure surges that,
45 if unmanaged, may damage infrastructure ([Xing & Sela, 2020](#)). Modal analysis offers a
46 systematic framework for capturing the dynamic behavior of WDSs, extending beyond fault
47 detection to improve the overall understanding of system response under various operating
48 conditions.

49 Existing approaches for transient and modal analysis in WDSs can be broadly classified into
50 time-domain simulation methods (e.g., the Method of Characteristics, MOC) and frequency-
51 domain formulations (e.g., the transfer-matrix or admittance-matrix methods, AMM) ([Lee et](#)
52 [al., 2006](#); [Lee et al., 2005](#); [Zecchin et al., 2009](#)). Frequency-domain methods express the
53 governing equations in the Laplace or Fourier domain to derive frequency response diagrams
54 (FRDs), which relate the input and output spectra of pressure and flow signals. The FRD
55 reveals resonance peaks that correspond to the natural frequencies of the system. The amplitude
56 of each peak reflects the damping of its associated mode, with larger peaks indicating poles
57 that lie closer to the imaginary axis and therefore represent more weakly damped oscillations
58 ([Zecchin et al., 2018](#)).

59 In this regard, several studies have demonstrated that the FRD of a single pipeline consists
60 of evenly spaced resonance peaks whose relative amplitudes depend on the measurement
61 location and are sensitive to leaks or blockages. In particular, Lee et al., ([Lee et al., 2005](#))
62 introduced inverse resonance and peak-sequencing methods to identify leaks by analyzing the
63 pattern of resonant peaks in the FRD, while Louati et al. ([Louati et al., 2020](#)) examined wave-
64 leak interactions and showed that leaks modify the relative magnitudes of resonance peaks

65 while leaving their frequencies largely unchanged. These studies established a clear frequency-
66 domain understanding of pipeline modes and their role in resonance phenomena.

67 Although these methods have proven effective in controlled or single-pipe systems, they are
68 fundamentally input–output based, relying on external excitation, transient simulation, or
69 spectral analysis of measured signals to infer modal content. For example, one can use the
70 MOC to generate pressure responses by applying a broadband excitation (e.g., a step or pulse)
71 and then compute the corresponding frequency response function via Fast Fourier Transform
72 (FFT) of the input–output signals ([Lee Pedro et al., 2008](#)). While this approach can reveal
73 dominant resonance frequencies, it requires long-duration simulations, careful design of the
74 input signal to excite all relevant modes, and sufficiently dense sensor coverage to capture
75 spatial variations. Moreover, the quality of the inferred modes depends on the signal-to-noise
76 ratio, sampling resolution, and how persistently each mode is excited. Repeating this process
77 across many operating points or measurement pairs quickly becomes computationally
78 demanding ([Che et al., 2021](#)).

79 In contrast, frequency-domain formulations such as the transfer-matrix method, determine
80 resonance by directly solving the linearized equations in the frequency domain, but these
81 methods provide only global input–output relationships and do not directly yield the internal
82 modal structure, that is, the mode shapes or how each pipe or node contributes to each
83 oscillation. Consequently, while FRD-based techniques offer valuable information on
84 resonance frequencies, they lack the ability to describe the spatial distribution of modal energy
85 within large, complex networks.

86 To overcome these challenges, this study introduces, for the first time, a state-space-based
87 framework for modal analysis of WDSs using the Elastic Water Column Model (EWCM). The
88 EWCM extends the Rigid Water Column Model (RWCM) by including the compressibility of

89 water and pipe-wall elasticity through a set of ordinary differential equations (ODEs), enabling
90 accurate simulation of fast transients while maintaining computational efficiency ([Imani et al.,](#)
91 [2025; Ulanicki & Beaujean, 2021; Zeng et al., 2022](#)). Unlike input–output approaches such as
92 the transfer-matrix method, the EWCM framework directly exposes the intrinsic dynamics of
93 the linearized system. The eigenvalues of the system matrix correspond to the natural modes
94 of the network, while the right and left eigenvectors describe how energy propagates through
95 the network and how each state variable participates in each oscillation mode. This state-space
96 formulation allows all modal information to be extracted in a single step, without requiring
97 excitation signals, frequency sweeps, or curve fitting.

98 A key advantage of this formulation is its compatibility with Participation Factor (PF)
99 analysis, which complements modal analysis by introducing spatial insight. PFs quantify the
100 contribution of each state variable, nodal head or flow rate—to each mode and reveal which
101 parts of the network are most dynamically involved. Originally developed for power-system
102 stability studies ([Abdulrahman, 2020; Abed et al., 2000](#)), PF analysis bridges the gap between
103 frequency and space: while frequency-domain diagrams show how a system behaves across
104 frequencies, PFs show where each mode is most active within the network. This capability
105 provides a powerful diagnostic tool for identifying spatially vulnerable regions that are prone
106 to resonance or amplified transients, information that cannot be obtained from classical
107 frequency-domain approaches.

108 This paper presents a time-domain approach to combined modal and PF analysis of WDSs
109 using the EWCM. The integration of these techniques allows not only for the extraction of
110 dynamic modes but also for the spatial identification of vulnerable locations where transients
111 may be amplified. This enables a more complete understanding of how hydraulic transients
112 affect WDSs and provides a new way to detect potential resonance behaviors in complex

113 networks. The goals of this study are fourfold. First, a state-space representation of WDSs is
114 developed by linearizing the EWCM around an operating point, enabling direct time-domain
115 modal analysis. Second, the system's natural modes are extracted through eigenvalue analysis
116 and validated against results obtained from the AMM in the frequency domain. Third,
117 participation factor analysis is applied to quantify the spatial contributions of flow and head
118 states to each mode, revealing critical locations that are more prone to amplifying transient
119 responses. Finally, the practical implications of PF analysis are verified through time-domain
120 simulations, including a real-world case study of the New York tunnel system subjected to
121 broadband excitations.

122 After establishing and verifying the mathematical foundation of the proposed modal analysis
123 framework, its potential applications are analogous to those of modal analysis in other
124 engineering domains. By identifying dominant modes and their spatial characteristics, the
125 framework can assist in surge protection assessment, guide sensor and actuator placement, and
126 support the development of reduced-order models for monitoring and control. The New York
127 tunnel test illustrates its practical use in a large-scale network, where complex interactions
128 between topology and dynamics can obscure regions of vulnerability. Together, modal and PF
129 analyses form a unified framework that links the mathematical structure of WDS dynamics to
130 physically interpretable spatial behavior and provides a foundation for future applications such
131 as real-time control and resilience assessment.

132 **Elastic Water Column Model**

133 The one-dimensional partial differential equations governing momentum and continuity in a
134 pressurized pipeline system are expressed as:

$$\frac{\partial h}{\partial x} + \frac{1}{gA} \frac{\partial q}{\partial t} + \frac{f q |q|}{2gDS^2} = 0 \quad (1)$$

$$\frac{gS}{a^2} \frac{\partial h}{\partial t} + \frac{\partial q}{\partial x} = 0 \quad (2)$$

135 where h represents the piezometric head, q is the volumetric flow rate, g is the gravitational
 136 acceleration, S is the internal cross-sectional area of the pipe, D is the pipe diameter, and f is
 137 the Darcy-Weisbach friction factor. The formulation of the EWCM originates from the analogy
 138 between hydraulic and electrical systems. The telegrapher's equation in electrical engineering
 139 shares the same mathematical form as the momentum and continuity equations in hydraulics.
 140 In this analogy, voltage corresponds to hydraulic head, current to flow rate, inductance to fluid
 141 inertia, resistance to pipe friction, and capacitance to the water compressibility. This
 142 correspondence forms the basis for representing hydraulic systems using an Electrical
 143 Equivalent Circuit (EEC) framework, which allows hydraulic energy storage, dissipation, and
 144 transfer to be analyzed in a physically intuitive way. When analyzing a pipe section of length
 145 l , under the assumption of constant hydraulic conditions (i.e., $\partial h/\partial x \approx \Delta h/l$ and $\partial q/\partial x \approx \Delta q/l$),
 146 the transient flow equations are reformulated following Souza et al. ([1999](#)):

$$\Delta h = -L \frac{\partial q}{\partial t} - R q |q| \quad (3)$$

$$\Delta q = -C \frac{\partial h}{\partial t} \quad (4)$$

147 where L is the hydraulic inductance $\left(L = \frac{l}{gS}\right)$, C is the hydraulic capacitance $\left(C = \frac{gSl}{a^2}\right)$, and R
 148 is the hydraulic resistance $\left(R = \frac{fl}{2gDS^2}\right)$. Ideally, the flow rate change due to water
 149 compressibility should be distributed evenly along the pipeline, but the Electrical Equivalent
 150 Method (EEM) simplifies this by concentrating the changes at specific points within the pipe

151 section. These points can be the center (T-shaped electrical circuit), the upstream end,
 152 downstream end, or both ends (π -shaped electrical circuit). Zeng et al. (2022) explored these
 153 configurations, and this study adopts the π -shaped electrical circuit for its efficiency in
 154 simulating the dynamic hydraulic behaviors with high accuracy. For such an EEM
 155 configuration, shown in Figure 1(a), the governing equations for the j th pipe segment are:

$$R'_j = R_j |q_j| \quad (5)$$

$$h_{j,u} = L_j \frac{dq_j}{dt} + R'_j q_j + h_{j,d} \quad (6)$$

$$\frac{c_j}{2} \frac{dh_{j,u}}{dt} = q_{j,u} - q_j = -\Delta q_{j,u} \quad (7)$$

$$\frac{c_j}{2} \frac{dh_{j,d}}{dt} = q_j - q_{j,d} = -\Delta q_{j,d} \quad (8)$$

156 where the subscript j refers to the j^{th} pipe segment in the network, and u and d represent the
 157 upstream and downstream ends, respectively. Eq. (6) follows Kirchoff's Voltage Law (KVL)
 158 for the EEC in Figure 1(a). In this equation, the sum of potential (head) losses due to inductance
 159 and resistance equals the head difference between two nodes. Using Eqs. (7) and (8), the
 160 continuity equation for a node, where multiple pipes converge, or demand exists, illustrated in
 161 Figure 1(b) is written as:

$$\sum_{j \in \Lambda_{i,d}} q_{j,d} - \sum_{j \in \Lambda_{i,u}} q_{j,u} + Q_i = 0 \quad (9)$$

162 where the sum $\sum_{j \in \Lambda_{i,d}} q_i$ represents the total inflow to node i from incoming pipes (set $\Lambda_{i,d}$),
 163 while $\sum_{j \in \Lambda_{i,u}} q_j$ represents the outflow from node i to outgoing pipes ($\Lambda_{i,u}$). Q_i represents the
 164 demand at node i . The sign of Q_i is positive where flow is directed toward the node, which is
 165 the opposite of the convention used by Zeng et al. (2022). This adjustment is made to maintain

166 consistency with the AMM, where the flow toward nodes is considered positive to ensure that
 167 the system remains energy passive, that is, it does not generate energy, in a theoretically
 168 consistent sense ([Zecchin, 2010](#)). The terms $\Delta q_{j,u}$ and $\Delta q_{j,d}$ denote flow rate changes at the
 169 node due to water compressibility and pipe elasticity, affecting both upstream and downstream
 170 pipes. These changes are critical for understanding fluid dynamics within the network,
 171 especially in response to variations in pressure and volume. The primary difference between
 172 the EWCM and RWCM models lies in these additional terms. Eq. (9) follows Kirchoff's
 173 Current Law (KCL), which enforces mass conservation at junctions by ensuring that the
 174 algebraic sum of inflows and outflows equals the nodal demand. Presenting the system in this
 175 circuit form provides an intuitive physical understanding of how hydraulic energy is stored,
 176 dissipated, and transmitted through the network. By substituting Eqs. (7) and (8) into Eq. (9),
 177 the following is obtained:

$$\left(\frac{1}{2} \sum_{j \in \Lambda_i} C_j\right) \frac{dh_i}{dt} = \sum_{j \in \Lambda_{i,d}} q_j - \sum_{j \in \Lambda_{i,u}} q_j + Q_i \quad (10)$$

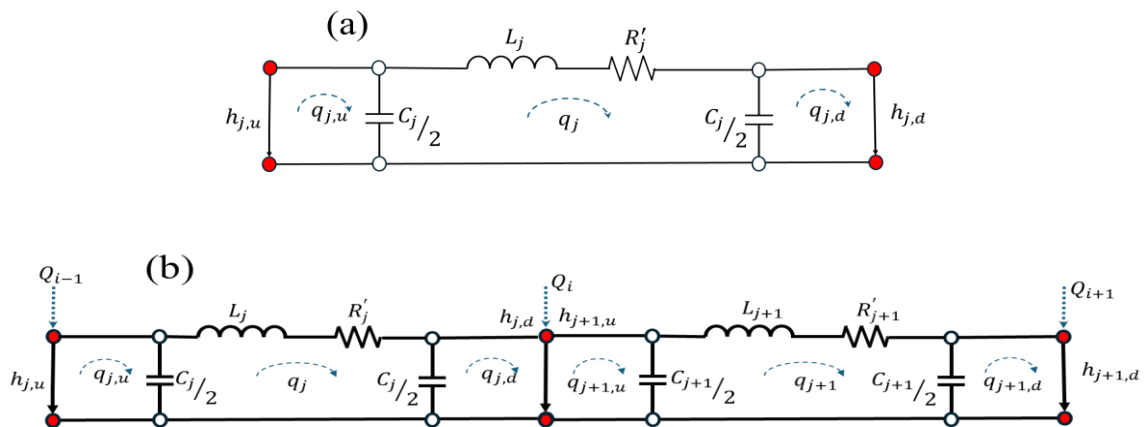


Figure 1. Electrical Equivalent Circuits: (a) EEC for a pipe segment; (b) EEC for two pipes in series.

178 ***Graph-Theoretical Formulation of WDSs***

179 In a WDS, the state variables include the hydraulic head at each node (except reservoirs) and
 180 the flow rates in the pipes. By determining these unknown variables, the entire system's state
 181 can be identified.

182 This paper represents a WDS as a graph of pipes. In graph theory, a graph is represented by an
 183 incidence matrix, \mathbf{M} , where each row corresponds to a node, and each column represents an
 184 edge element. The matrix entries are either 1, -1, or 0, depending on the relationships between
 185 nodes and edges. A value of 1 in $\mathbf{M}_{i,j}$ indicates that edge j exits node i , a value of -1 means
 186 edge j enters node i , and 0 signifies no connection between node i and edge j . Dividing nodes
 187 into internal and reservoir nodes (boundary nodes) allows us to partition the incidence matrix
 188 as:

$$\mathbf{M} = \begin{bmatrix} \mathbf{M}_I \\ \mathbf{M}_R \end{bmatrix} \quad (11)$$

189 where the subscript I refers to internal nodes and R to reservoir nodes. Similarly, the nodal head
 190 vector is partitioned as:

$$\mathbf{h} = \begin{bmatrix} \mathbf{h}_I \\ \mathbf{h}_R \end{bmatrix} \quad (12)$$

191 where \mathbf{h}_I represents the heads at internal nodes, and \mathbf{h}_R corresponds to the heads at reservoir
 192 nodes. Based on these partitions, the vector of head differences $\Delta\mathbf{h}$ across each element is
 193 expressed as:

$$\Delta\mathbf{h} = \mathbf{M}\mathbf{h} = \begin{bmatrix} \mathbf{M}_I \\ \mathbf{M}_R \end{bmatrix}^T \begin{bmatrix} \mathbf{h}_I \\ \mathbf{h}_R \end{bmatrix} \quad (13)$$

194 The head differences across pipes are derived from the incidence matrix and the nodal pressure
 195 head vector. As in Zeng et al. (2022), the demand vector \mathbf{Q} and parameter matrices \mathbf{L} , \mathbf{R} , \mathbf{C} ,

196 and \mathbf{T} (all diagonal) are employed in formulating the momentum and continuity equations for
 197 the pipes. The momentum equation is then written as:

$$\mathbf{L} \frac{d\mathbf{q}}{dt} = -\mathbf{R} \text{diag}\{|\mathbf{q}|\}\mathbf{q} + \mathbf{M}_I^T \mathbf{h}_I + \mathbf{M}_R^T \mathbf{h}_R \quad (14)$$

198 where $|\mathbf{x}|$ is the element-wise vector or matrix of \mathbf{x} . The continuity equation at the nodes is
 199 given by:

$$\frac{1}{2} \text{diag}\{|\mathbf{M}_I| \text{vec}\{\mathbf{C}\}\} \frac{d\mathbf{h}_I}{dt} = \mathbf{M}_I \mathbf{q} + \mathbf{Q} \quad (15)$$

200 where $\text{vec}(\text{Xing \& Sela})$ is here defined as the vector of the diagonal elements of matrix \mathbf{X} . Eq.
 201 (14) and (15) form a system of nonlinear ODEs for WDSs. This set of equations has been
 202 validated with MOC and the detail of the discretization of pipes can be found in the Zeng et al.
 203 (2022) and (Imani et al., 2025).

204 *Nonlinear System Representation*

205 The system of equations above can be compactly written in a state-space form. To do this, the
 206 state vector \mathbf{x} is defined to include both the flow rates through the pipes and the hydraulic heads
 207 at the internal nodes:

$$\mathbf{x} = \begin{bmatrix} \mathbf{q} \\ \mathbf{h}_I \end{bmatrix} \quad (16)$$

208 The inputs \mathbf{u} to the system are the hydraulic heads at the reservoirs and the external demands:

$$\mathbf{u} = \begin{bmatrix} \mathbf{h}_R \\ \mathbf{Q} \end{bmatrix} \quad (17)$$

209 In this format, the system's nonlinear dynamics can be represented as:

$$\dot{\mathbf{x}} = f(\mathbf{x}, \mathbf{u}) \quad (18)$$

210 This equation describes how the state vector \mathbf{x} evolves over time as a nonlinear function
211 $f(\mathbf{x}, \mathbf{u})$ of the state and the inputs. Solving this equation gives the complete transient response
212 of the WDS to changes in demand or reservoir head, capturing both the flow rates and heads
213 in the network.

214 **Modal Analysis and Participation factor**

215 The following sections outline the key components of the proposed approach. First, the EWCM
216 is linearized to obtain a state-space model suitable for modal analysis. Then, eigenvalue
217 analysis and participation factor computations are performed to extract the system modes and
218 assess their spatial characteristics. The AMM is also introduced in the frequency domain, and
219 its methodology is compared with the mode extraction process based on the EWCM.

220 ***Linearization and state-space representation***

221 To analyze the system using modal and frequency-domain methods, it's necessary to linearize
222 the nonlinear system around an operating point. This is particularly useful for stability analysis,
223 control design, and understanding the dominant modes of the system ([Franklin et al., 2010](#)). In
224 practice, the operating point corresponds to the steady-state heads and flows obtained from a
225 calibrated hydraulic model or from SCADA data under normal operating conditions. This state
226 reflects the nominal behavior of the network. If alternative regimes (such as peak-demand or
227 low-demand operation) are of interest, the same procedure can be repeated to obtain a family
228 of linearized models that describe how modal properties vary across different operating

229 conditions. Linearization involves approximating the nonlinear system with a linear one by
 230 expanding $f(\mathbf{x}, \mathbf{u})$ in a Taylor series around the steady-state operating point \mathbf{x}_0 and \mathbf{u}_0 . This
 231 assumes that flow and head perturbations are small compared to their nominal values. This
 232 yields the linearized state-space representation of the WDS:

$$\dot{\mathbf{x}} = \mathbf{A}\mathbf{x} + \mathbf{B}\mathbf{u} \quad (19)$$

233 where \mathbf{A} and \mathbf{B} are the Jacobian matrices of partial derivatives with respect to the state and
 234 input, respectively. Matrix \mathbf{A} is the system matrix, which captures how the state variables (flow
 235 rates and hydraulic heads) change in response to perturbations in the state. Matrix \mathbf{B} is the input
 236 matrix, which describes how external inputs (such as reservoir heads or demands) influence
 237 the state variables.

$$\mathbf{A} = \begin{pmatrix} \mathbf{L}^{-1}\mathbf{R}\text{diag}\{|\mathbf{q}|\} & \mathbf{L}^{-1}\mathbf{M}_I^T \\ 2\text{diag}\{|\mathbf{M}_I|\text{vec}\{\mathbf{C}\}\}^{-1}\mathbf{M}_I & \mathbf{0}_{m \times m} \end{pmatrix} \quad (20)$$

238 where $\mathbf{0}_{m \times m}$ is an $m \times m$ matrix of zeros, and $\mathbf{L}^{-1}\mathbf{R}\text{diag}\{|\mathbf{q}|\}$ is clearly a diagonal matrix. Here,
 239 m denotes the number of internal nodes. The system matrix \mathbf{A} is crucial for understanding the
 240 dynamic behavior of the WDS. Its eigenvalues determine the natural modes of the system,
 241 while the eigenvectors provide insight into how different components of the system interact
 242 with each mode.

243 *Eigenvalue Analysis and participation factor*

244 The eigenvalues λ_i of the system matrix \mathbf{A} are found by solving the characteristic equation:

$$\det\{\mathbf{A} - \lambda_i \mathbf{I}\} = 0 \quad (21)$$

245 Each eigenvalue represents a mode of the system. If λ_i is real, the mode is non-oscillatory, and
 246 its sign determines whether the mode is stable ($\lambda_i < 0$) or unstable ($\lambda_i > 0$). Complex

247 eigenvalues correspond to oscillatory modes, where the real part σ_i determines the stability and
 248 the imaginary part ω_i corresponds to the oscillation frequency:

$$\lambda_i = \sigma_i + \mathbf{i}\omega_i \quad (22)$$

249 where \mathbf{i} is the imaginary unit. For each eigenvalue, there are corresponding right and left
 250 eigenvectors, \mathbf{v}_i and \mathbf{w}_i . The right eigenvector v_i satisfies:

$$A v_i = \lambda_i \mathbf{v}_i \quad (23)$$

251 and represents the mode shape, describing how the state variables (flow rates and heads)
 252 contribute to the dynamics of mode i . The left eigenvector w_i satisfies:

$$\mathbf{w}_i^T A = \lambda_i \mathbf{w}_i^T \quad (24)$$

253 and indicates how the mode i can be observed in the outputs. The PF p_{ki} for the k -th state
 254 variable in the i -th mode is defined as ([Abdulrahman, 2020](#); [Garofalo et al., 2002](#)):

$$p_{ki} = \frac{\|v_{ki}\| \|w_{ki}\|}{\sum_{k=1}^n \|v_{ki}\| \|w_{ki}\|} \quad (25)$$

$$\bar{p}_{ki} = \frac{p_{ki}}{\max_{i=1,\dots,n} |p_{ki}|} \quad (26)$$

255 where $\| . \|$ denotes the L_1 -norm operator, n is the total number of state variables, and \bar{p}_{ki} is the
 256 normalized participation factor. These factors quantify how much the k -th state variable
 257 contributes to the i -th mode, combining information from both the left and right eigenvectors.
 258 PFs have key properties that make them valuable for system analysis. First, the sum of PFs for
 259 each mode across all state variables equals 1, meaning all variables together represent the full
 260 dynamics of that mode. Similarly, the sum for each state variable across all modes also equals
 261 1, indicating the state variable contributes fully to the system's overall behavior ([Abed et al.,](#)

262 [\(2000\)](#). Additionally, PFs reveal how sensitive eigenvalues are to changes in system parameters,
 263 helping to identify critical components for control and design decisions.

264 ***Admittance Matrix Method for Mode Extraction***

265 In the AMM, the dynamic behavior of a WDS is analyzed in the Laplace domain. The detailed
 266 methodology can be found in ([Zecchin, 2010](#)). This method applies the Laplace transform to
 267 the continuity and momentum equations to convert the equations from the time domain to the
 268 frequency domain with the Laplace operator s . The Laplace operator $s = \sigma + i\omega$, where σ
 269 represents the decay rate, and ω represents the frequency. The WDS is then modeled using an
 270 admittance matrix $\mathbf{Y}(s)$, which relates the nodal heads $\mathbf{h}(s)$ (the Laplace transform of \mathbf{h}) and
 271 flows $\mathbf{Q}(s)$ (the Laplace transform of the demands and reservoir flows) at each node. The
 272 admittance matrix is constructed as follows ([Zecchin et al., 2018](#)):

$$\mathbf{Y}(s)\mathbf{h}(s) = \mathbf{Q}(s) \quad (27)$$

$$\mathbf{Y}(s) = (\mathbf{N}_u \quad \mathbf{N}_d) \begin{pmatrix} \mathbf{Z}_c^{-1}(s)\coth\Gamma(s) & -\mathbf{Z}_c^{-1}(s)\operatorname{csch}\Gamma(s) \\ -\mathbf{Z}_c^{-1}(s)\operatorname{csch}\Gamma(s) & \mathbf{Z}_c^{-1}(s)\coth\Gamma(s) \end{pmatrix} (\mathbf{N}_u \quad \mathbf{N}_d)^T \quad (28)$$

273 Where \mathbf{N}_u and \mathbf{N}_d are the upstream and downstream incidence matrices, respectively, and
 274 contain the information regarding the topology of the system. These matrices have the
 275 following relation with the incidence matrix from the previous sections:

$$\mathbf{N}_u = \frac{\mathbf{M} + |\mathbf{M}|}{2} \quad (29)$$

$$\mathbf{N}_d = \frac{|\mathbf{M}| - \mathbf{M}}{2} \quad (30)$$

276 In Eq. 27, $\Gamma(s)$ is the propagation operator, and $\mathbf{Z}_c(s)$ is the characteristic impedance (see
 277 ([Zecchin et al., 2009](#))for details).

278 By partitioning the system into controlled nodes (inputs) and free nodes (outputs), the network
 279 matrix Eq. (27) can be rewritten in the following partitioned form ([Zecchin et al., 2009](#)):

$$\begin{pmatrix} \mathbf{Y}_d(s) & \mathbf{Y}_{d-r}(s) \\ \mathbf{Y}_{r-d}(s) & \mathbf{Y}_r(s) \end{pmatrix} \begin{pmatrix} \mathbf{h}_I(s) \\ \mathbf{h}_R(s) \end{pmatrix} = \begin{pmatrix} \mathbf{Q}(s) \\ \mathbf{Q}_R(s) \end{pmatrix} \quad (31)$$

280 where \mathbf{Q}_R are the Laplace transform of reservoir flows (positive flow is into the network),
 281 $\mathbf{Y}_d(s)$ is the $n_d \times n_d$ system matrix representing the demand nodes, and $\mathbf{Y}_r(s)$ is the $n_d \times n_d$
 282 system matrix representing the reservoir nodes. $\mathbf{Y}_{d-r}(s)$ and $\mathbf{Y}_{r-d}(s)$ are the respective
 283 partitions of the network matrix that describe the contributions of flow at the demand nodes
 284 and reservoir nodes, resulting from the nodal heads at the opposite set of nodes. It is important
 285 to note that $\mathbf{Y}_d(s)$ and $\mathbf{Y}_r(s)$ are symmetric, and $\mathbf{Y}_{d-r}(s) = \mathbf{Y}_{r-d}^T(s)$.

286 The transfer function is then derived based on this partitioning. Zecchin et al. (2009) formulated
 287 expressions for the input-output (I/O) transfer function as follows.

$$\begin{aligned} \mathbf{H}(s) &= \begin{pmatrix} \mathbf{H}_{11}(s) & \mathbf{H}_{12}(s) \\ \mathbf{H}_{21}(s) & \mathbf{H}_{22}(s) \end{pmatrix} \\ &= \begin{pmatrix} -\mathbf{Y}_d^{-1}(s)\mathbf{Y}_{d-r}(s) & \mathbf{Y}_d^{-1}(s) \\ \mathbf{Y}_r(s) - \mathbf{Y}_{r-d}(s)\mathbf{Y}_d^{-1}(s)\mathbf{Y}_{d-r}(s) & (\mathbf{Y}_d^{-1}(s)\mathbf{Y}_{d-r}(s))^T \end{pmatrix} \end{aligned} \quad (32)$$

288 For modal analysis, the system's transfer function is expressed in a mode-based form, where
 289 the system's dynamics are described by a sum of modal terms ([Zecchin et al., 2018](#)):

$$G(s) = \sum_{n=1}^N \left(\frac{G_n}{s - z_n} + \frac{G_n^*}{s - z_n^*} \right) \quad (33)$$

290 where N represents the number of modes, G_n is the complex-valued modal coefficient matrix
291 for the n -th mode, and $z_n = \sigma_n + i\omega_n$ is the complex frequency for the n -th mode. The operator
292 * denotes the complex conjugate.

293 To compute the modes, the poles of the transfer function $G(s)$ must be located in the complex
294 plane. These complex modal frequencies correspond to the singular points of G , where
295 $\{z \in \mathbb{C} : |G_{(z)}| = 1\}$. To determine the complex frequencies z_n , it is necessary to identify the
296 locations of the poles in the analytic I/O transfer function $H(s)$.

297 The general process of finding the complex frequencies z_n involves determining bounds for
298 their real and imaginary components (i.e., $\sigma_n \in [\sigma_{min}, \sigma_{max}]$ and $\omega_n \in [\omega_{min}, \omega_{max}]$),
299 followed by locating z_n by identifying the maxima of the elements of $|H|$ within these bounds,
300 which correspond to the pole locations. The process for finding the pole locations can be found
301 in ([Zecchin et al., 2018](#)).

302 ***Comparison of AMM and EWCM in Modal Analysis***

303 Modal information can, in principle, be obtained using several classical approaches. In the time
304 domain, the MOC can be used by exciting the system, recording the pressure and flow
305 responses at discrete nodes, and performing Fourier or Laplace transforms to construct
306 frequency-response functions. The locations of the poles in the Laplace plane can then be
307 inferred from the resonance peaks, poles located closer to the imaginary axis correspond to
308 larger amplitude responses. While this approach is conceptually straightforward, it becomes
309 computationally demanding for large-scale networks, as multiple transient simulations are
310 required to capture the full spatial response.

311 Similarly, the Transfer Matrix Method (TMM), which is formulated in the frequency domain,
312 allows the transfer function of a single pipe or a simple series system to be constructed and its
313 FRD obtained, from which the poles can also be inferred. However, the traditional TMM
314 formulation is primarily developed for single-pipe systems, and extending it to general network
315 configurations requires additional derivations. For this reason, the AMM is used in this study
316 as the benchmark for comparison. The AMM is formulated in the Laplace domain, and an
317 established framework exists for extracting poles for arbitrary network topologies.

318 The AMM and the EWCM both offer distinct advantages in the modal analysis of water
319 distribution systems, depending on the context and objectives of the analysis. The AMM is
320 efficient for analysing the system's input–output relationships and allows quick identification
321 of resonance frequencies by constructing the frequency-response function. Extracting modes
322 from the AMM, however, requires specific steps such as sweeping through a frequency range
323 and locating poles, which can involve additional computational effort. Despite this, it remains
324 a reliable approach for understanding a system's dynamic characteristics in the frequency
325 domain.

326 The EWCM, in contrast, operates in the time domain and provides a model based on ODEs
327 that approximate the underlying PDEs of unsteady flow. When linearized about a steady
328 operating point, the EWCM yields a state-space representation in which modal information
329 follows directly from the eigenvalues and eigenvectors of the system matrix. This provides
330 direct access to both right and left eigenvectors, enabling the computation of PFs and detailed
331 spatial interpretation of each mode, capabilities that are not directly available from frequency-
332 domain approaches such as the AMM. These distinctions reflect the classical difference
333 between transfer-function models and state-space models described in control theory texts

334 (e.g., ([Franklin et al., 2010](#))): transfer-function formulations capture input–output behaviour,
335 while state-space models also expose the internal dynamics of the system.

336 Numerical simulation

337 In this section, three test cases are presented to demonstrate the application of the modal
338 analysis and PF analysis framework developed for WDS using the EWCM. The first test case
339 focuses on a single pipeline to explore the fundamental behaviors and validate the extracted
340 modes using both the EWCM and the AMM. The second test case extends the analysis to a
341 pipe network, introducing complexities such as loops and multiple internal nodes. For these
342 two test case, eigenvalue analysis and PF analysis are employed to extract the system modes
343 and assess the contributions of different system states to each mode. Time-domain simulations
344 are used to further verify the results. In Test Case 3, a real world test case, New York tunnel
345 has been chosen to show the applicability of PF in revealing critical locations due to hydraulic
346 transients.

347 *Test case 1: single pipeline*

348 In this test case, the modal analysis for a single pipeline, as shown in Figure 2 , is presented.

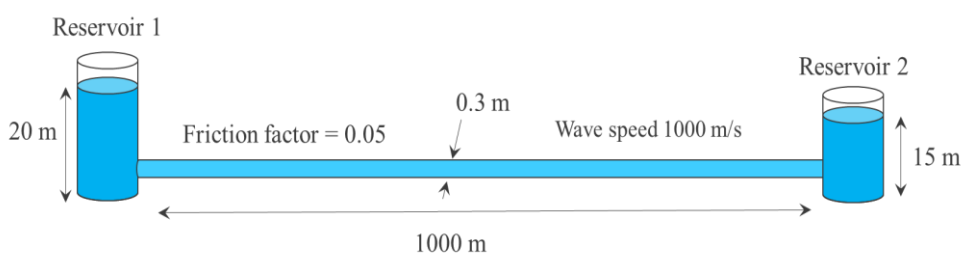


Figure 2. Structure of the pipeline for test case 1.

349

350 To begin with, the EWCM is used to determine the modes, where the spatial discretization is
 351 governed by the critical frequency ($f_c = a/10l$). The segment length l is chosen such that the
 352 highest frequency of interest satisfies $f_{max} \leq f_c$. In this test case, a maximum frequency of 10
 353 rad/s was considered; using this value, the corresponding critical frequency was applied to
 354 determine the appropriate pipe-segment length and, consequently, the number of reaches for
 355 each pipe. As a result, the pipeline was discretized into 16 reaches. Based on this discretization,
 356 the system matrix has a dimension of 31×31 , where 16 states correspond to flow rates and
 357 15 states correspond to the pressure heads at internal nodes. Performing eigenvalue analysis on
 358 this matrix yields 31 eigenvalues, which are listed in Table 1.

359 **Table 1.** Eigenvalue of system matrix for test case 1

Number	Eigenvalue	Number	Eigenvalue
1	-0.1278	16,17	$-0.0639 \pm 22.627i$
2,3	$-0.0639 \pm 3.135i$	18,19	$-0.0639 \pm 24.736i$
4,5	$-0.0639 \pm 6.242i$	20,21	$-0.0639 \pm 26.606i$
6,7	$-0.0639 \pm 9.288i$	22,23	$-0.0639 \pm 28.221i$
8,9	$-0.0639 \pm 12.245i$	24,25	$-0.0639 \pm 29.564i$
10,11	$-0.0639 \pm 15.084i$	26,27	$-0.0639 \pm 30.622i$
12,13	$-0.0639 \pm 17.778i$	28,29	$-0.0639 \pm 31.385i$
14,15	$-0.0639 \pm 20.300i$	30,31	$-0.0639 \pm 31.845i$

360 As observed in Table 1, there is one pole with no imaginary part, representing a damped mode
 361 without an oscillatory component. This damped pole can also be found using the RWCM. For
 362 a single pipeline with a fixed head, the equation for this pole is given by $\frac{fa|q_0|}{l_{DS}}$, and the detailed
 363 derivation for obtaining this damped mode through the RWCM is provided in Appendix. The
 364 remaining poles have both real and imaginary parts. For this single pipeline, all oscillatory
 365 modes have equal real parts and are complex conjugates, meaning that their decay rates are
 366 identical, with differences only in their imaginary components. The real part of the poles is

367 influenced by the system's resistance, while the fluid compressibility modelled as capacitance
368 in EWCM impacts the imaginary part.

369 To verify the pole locations, the mode extraction procedure using the AMM was also applied
370 to this pipeline. The transfer function surface is shown in Figure 3, where the local maxima
371 indicate the locations of the poles. By performing a 2D optimization, the exact pole locations
372 were extracted, as shown in Figure 4. It is important to note that only the positive frequencies
373 are displayed in Figure 3 and Figure 4 for clarity. A comparison of the pole locations obtained
374 by both methods reveals that the poles from the EWCM match those from the AMM up to the
375 critical frequency. Beyond this frequency, the EWCM's poles diverge from the actual poles.
376 However, by increasing the discretization, the bandwidth can be expanded, allowing the
377 EWCM to capture higher-frequency modes. Additionally, the location of the damped mode is
378 in agreement across all three models EWCM, RWCM, and the AMM.

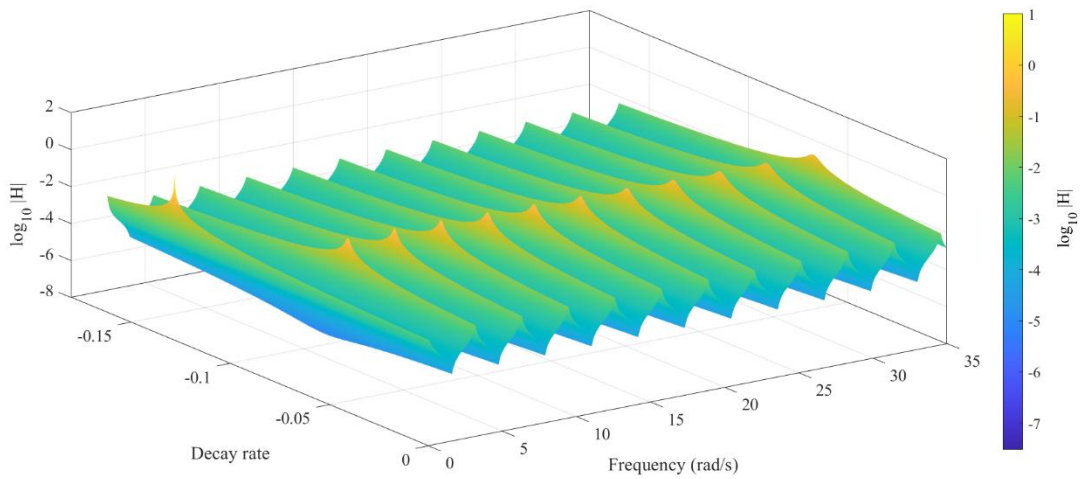


Figure 3. The surface of the absolute value of the Laplace-domain response surface for test case 1.

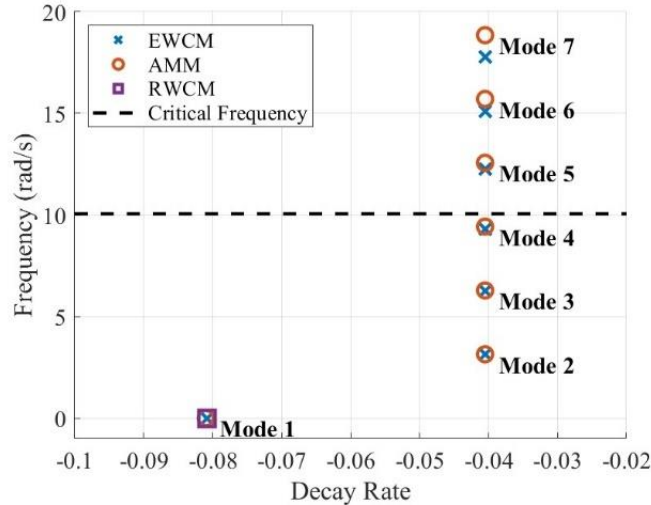


Figure 4. locations in the Laplace domain for Test Case 1.

379 By obtaining the eigenvalues along with the left and right eigenvectors, the PF matrix can be
 380 constructed for this test case. In this matrix, the rows correspond to the system states, and the
 381 columns represent the modes. Since only modes 1 to 4 are valid (represented in Figure 4), the
 382 PFs for these modes are extracted and shown in Figure 5. A PF of 1 indicates the highest
 383 participation of a state in a given mode, while a value of 0 signifies no participation. Mode 1
 384 represents the damped mode, and only the flow state variables contribute to this mode, with all
 385 variables having equal importance. This result can be verified using the RWCM, as in this
 386 model, the left-hand side of Eq. (10) is zero, meaning there is no partial derivative of the
 387 internal head over time. For the other oscillatory modes, the PFs are illustrated in Figure 6
 388 (only for modes with positive imaginary parts).

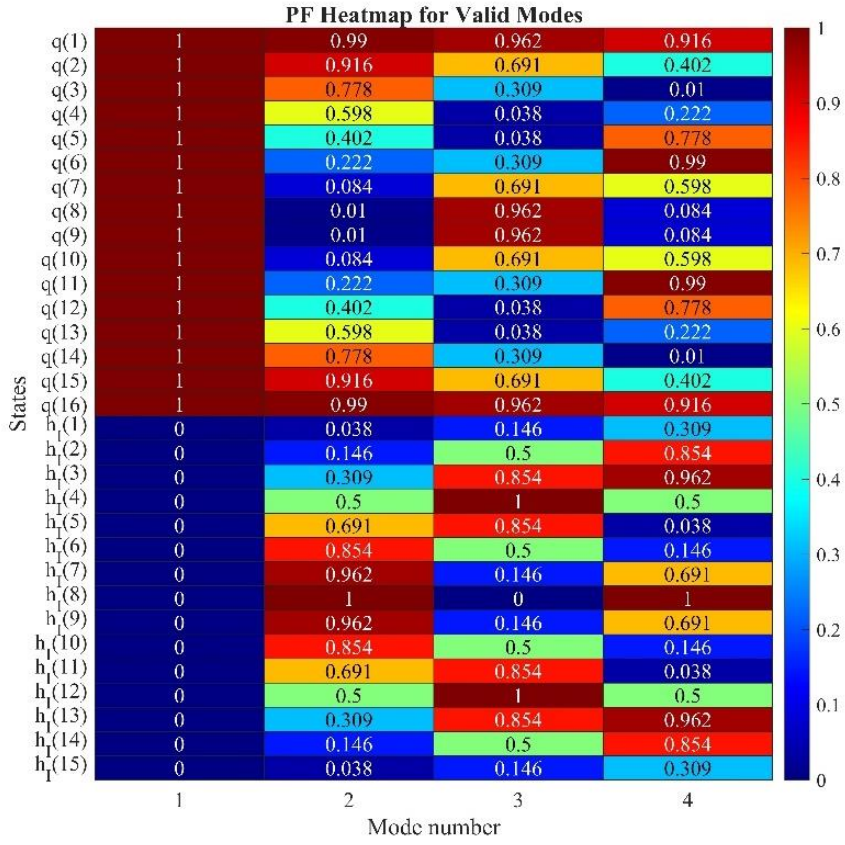


Figure 5. Participation matrix for valid modes.

389 In Figure 6, the modes shown correspond to the first three harmonics of the system. For the
 390 mode 2, the PF for the internal head variable is highest at the center of the pipe. This behavior
 391 can be understood by drawing an analogy to systems such as a mass-spring-damper or a
 392 vibrating string fixed at both ends. In the first harmonic of the system, there is an antinode at
 393 the center of the pipe, where the potential energy is maximized, similar to the maximum
 394 displacement in a vibrating string. The two fixed heads at the pipe's input and output act as
 395 nodes, where the displacement is zero. This pattern can be extended to the higher harmonics,
 396 represented by modes 2 and 3 (the second and third harmonics of the pipeline). In these modes,
 397 additional nodes and antinodes appear along the length of the pipe, with the internal head
 398 variable participating more significantly at certain points, depending on the mode shape. These
 399 harmonics have been explained in detail by ([Wylie, 1993](#)).

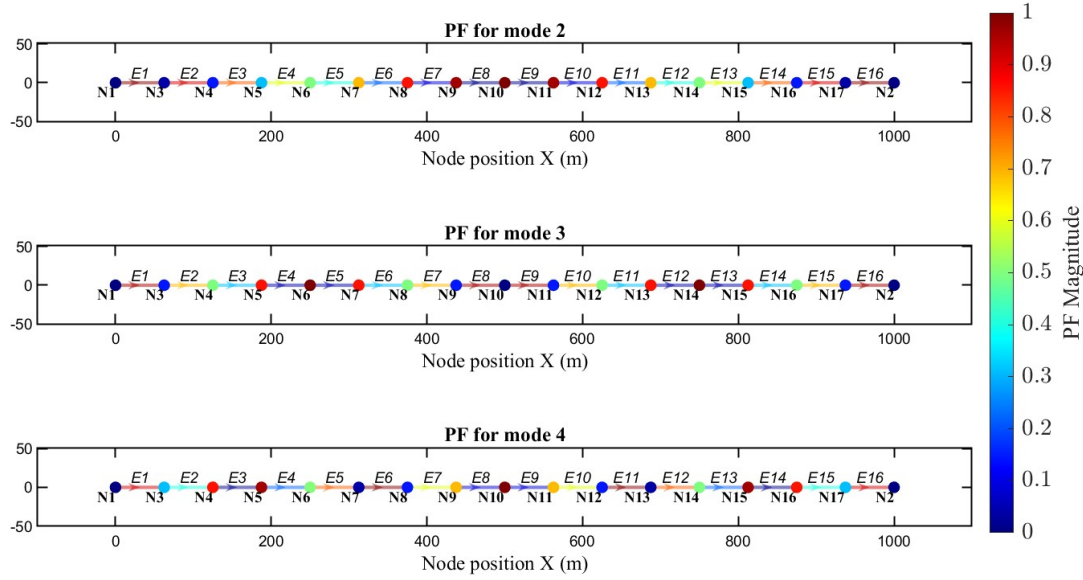


Figure 6 Representation of PFs on the pipeline: nodes are associated with participation of nodal heads, and edges are associated with flow rates through pipes.

400 To verify the PF matrix and identify the most sensitive locations for each mode, a time-domain
 401 simulation was performed. The system was excited at the location with the highest PF, with
 402 the excitation frequency matching the mode frequency. To excite the system at point 6 (Node
 403 numbering in Figure 6), which exhibits the highest PF for the second oscillatory mode (-0.0639
 404 $\pm 6.242i$), an oscillatory demand, given by the equation below, was used.

$$Q(t) = 0.01 + 0.0005 \times \sin(6.242t) \quad (34)$$

405 In Eq. (34), the constant term ($0.01 \text{ m}^3/\text{s}$) represents the steady-state demand, while the
 406 oscillatory term ($0.0005 \text{ m}^3/\text{s} = 0.5 \text{ L/s}$) was chosen as 5% of the nominal demand. This
 407 amplitude ensures that the excitation remains within the linear range of the model while later
 408 allowing the analysis to demonstrate the system's sensitivity, where even such a small
 409 perturbation can lead to noticeable pressure variations depending on the excitation location.
 410 The simulation results, after reaching a steady oscillatory state, are shown in Figure 7, which
 411 illustrates the variation of pressure at internal nodes ($h(t) - h_0$). It can be seen that a small

412 variation in demand (0.5 L/s) causes a head change of approximately 10 m at nodes 6 and 14,
 413 which correspond to the locations with the highest PF values. From Figure 6, node 10 has the
 414 lowest PF for the second oscillatory mode, and the time-domain simulation in Figure 7
 415 confirms that this node exhibits the smallest oscillation amplitude under steady oscillatory
 416 conditions.

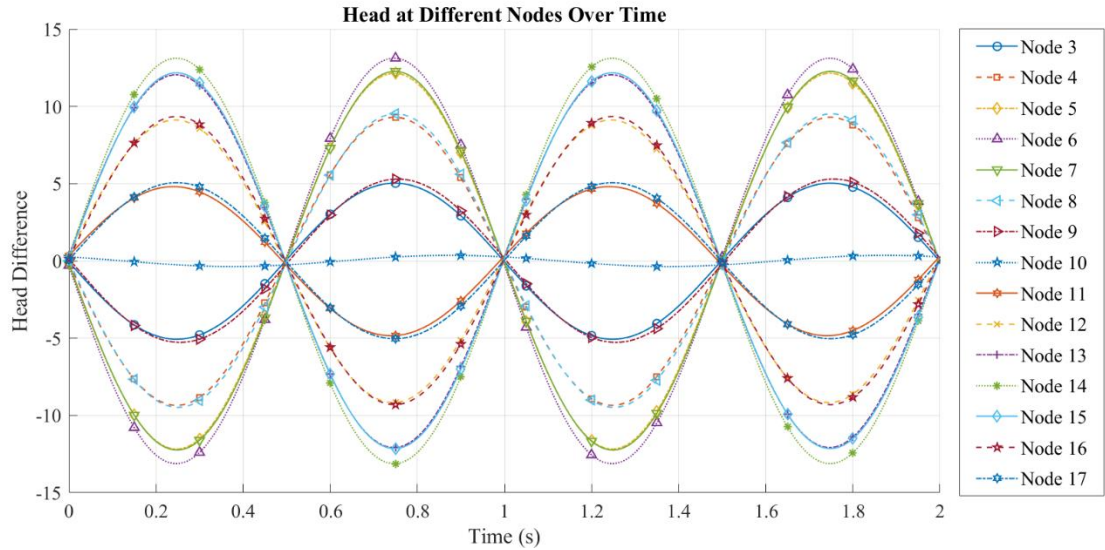


Figure 7. Head changes at all internal nodes under steady oscillatory conditions, with the excitation point at node 6.

417 To further demonstrate the influence of excitation location, the demand oscillation was next
 418 applied at the lowest-PF node (node 10) for the same mode, using the same excitation defined
 419 in Eq. (34). The resulting head variations, shown in Figure 8, indicate that the maximum head
 420 change was less than 0.4 m, significantly smaller than the response observed when exciting at
 421 the high-PF location. This comparison shows that identical excitations can lead to markedly
 422 different dynamic responses depending on the spatial location of the applied disturbance. When
 423 the excitation is applied at a high-PF node, the pressure response is amplified due to resonance
 424 with the corresponding mode, whereas excitation at a low-PF node produces only a weak
 425 response that is rapidly attenuated. The spatial pattern of the simulated head amplitudes in

426 Figure 9 closely matches the PF distribution in Figure 6, illustrating that the regions with higher
 427 PF values experience greater oscillation amplitudes under modal excitation. This agreement
 428 verifies that the PFs capture the underlying spatial characteristics of the oscillatory modes
 429 observed in the time-domain simulation.

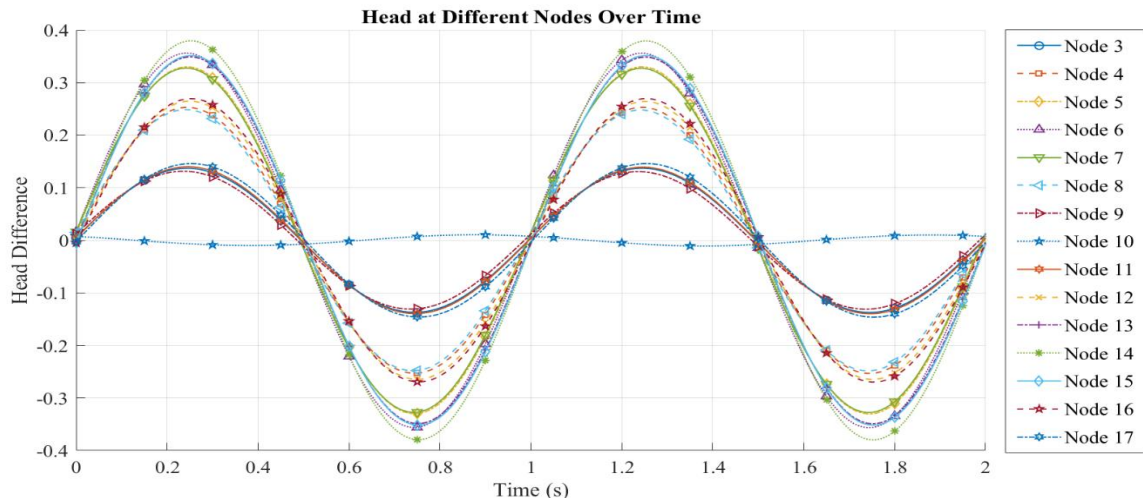


Figure 8. Head changes at all internal nodes under steady oscillatory conditions, with the excitation point at node 10.

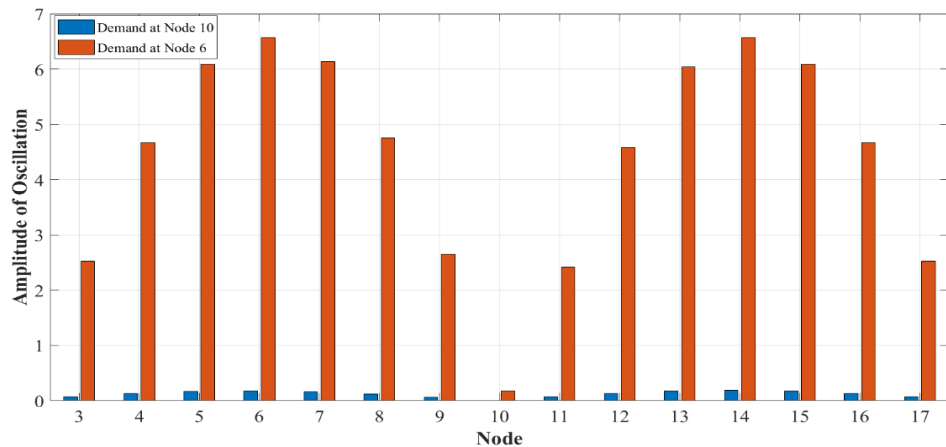


Figure 9. FFT of internal node heads, with the excitation point at node 6 and 10.

430 **Test case 2: Pipe network**

431 In this test case, the modal analysis for the pipe network shown in Figure 10 is implemented.
 432 The system contains one loop, where all the details are provided in Figure 10. In the first step,
 433 the pole locations were identified using both the EWCM and the AMM, as shown in Figure 11.
 434 The number of reaches in the system was chosen so that there is one reach every 100 meters in
 435 the system. Therefore, the number of reaches for the pipes is 5, 4, 6, 5, 5 and 2 respectively.

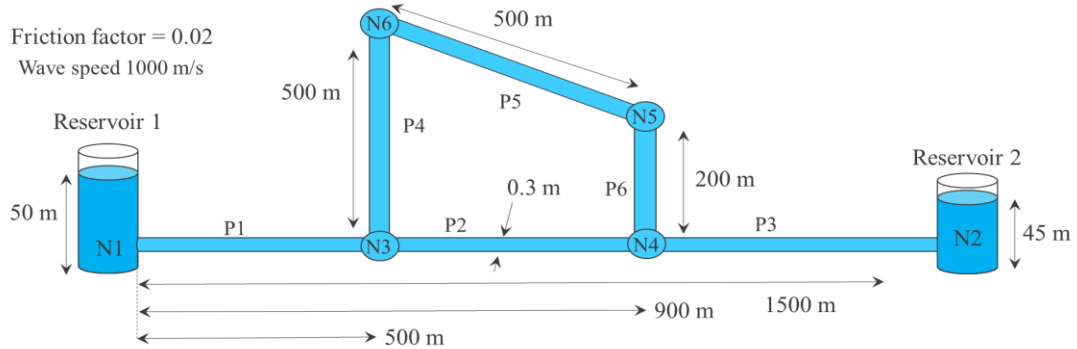


Figure 10. Network structure for Test Case 2.

436 In Figure 11, by neglecting the poles that lie on the critical frequency line, there are only four
 437 oscillation modes below the critical frequency. In this system, there are two damped modes,
 438 were also identified by the RWCM. According to ([Shimada, 1992](#)), the number of independent
 439 states is equal to the difference between the number of pipes and the number of internal nodes.
 440 In this case, the system has 6 pipes and 4 internal nodes, resulting in two negative real poles.
 441 These damped modes are associated with the loop and the spanning tree between the two
 442 reservoirs. As can be seen, all poles below the critical frequency align closely for both the
 443 EWCM and AMM. A slight deviation is observed for Mode 4, for which the relative error is
 444 below 1%. This small difference arises from the grid resolution and the optimization procedure
 445 used in the AMM to identify modal poles.

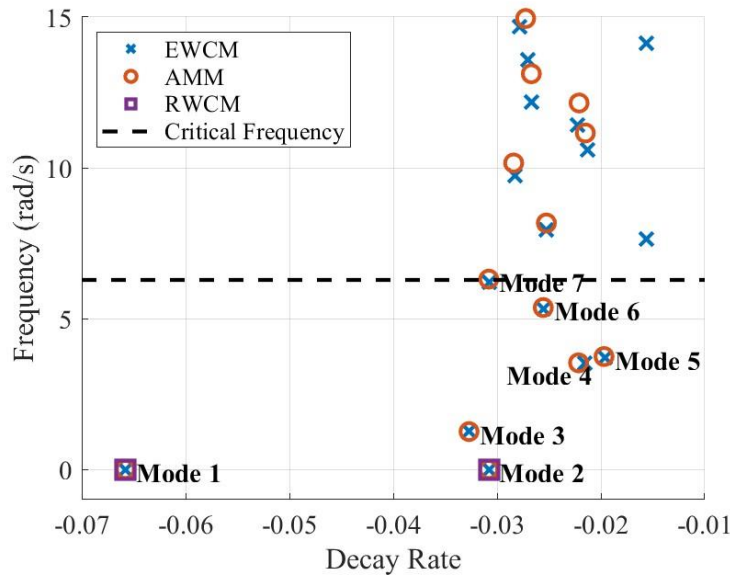


Figure 11. Pole locations for Test Case 2.

446 The 3D surface of the transfer function in the Laplace domain, obtained using the AMM, is
 447 shown in Figure 12. The line with a decay rate equal to zero represents the FRD of the system
 448 between the input and output. The location of the poles affects the FRD of the system.

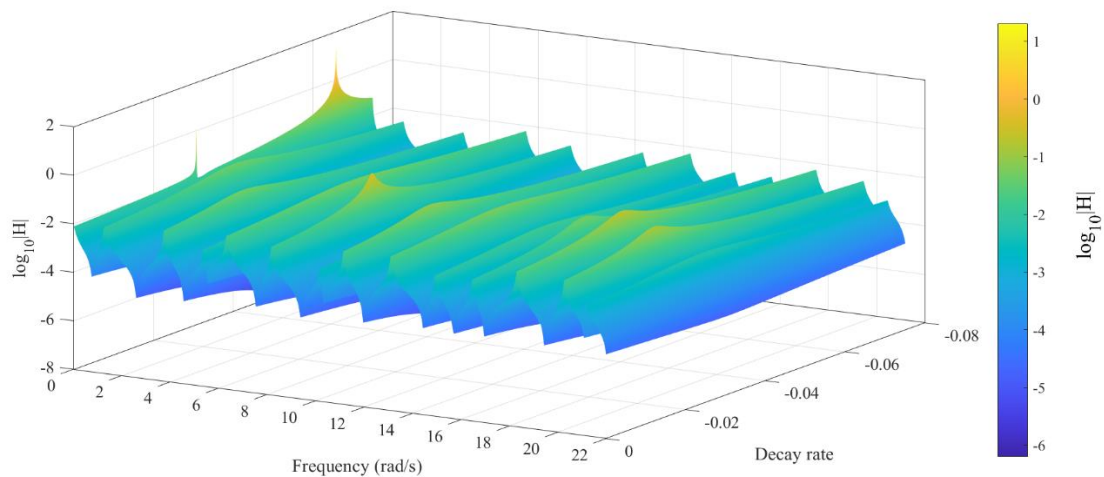


Figure 12. Surface plot of the Laplace-domain response for Test Case 2.

449 Figure 13 shows the PFs for all valid modes. As seen in Figure 13 (a) and (b), for the two
 450 damped modes, only the flow rate states participate in the modes, as indicated by the dark blue

451 colour in the links representing flow variables. The flow rate states of Pipe 2 participate in both
 452 damped modes.

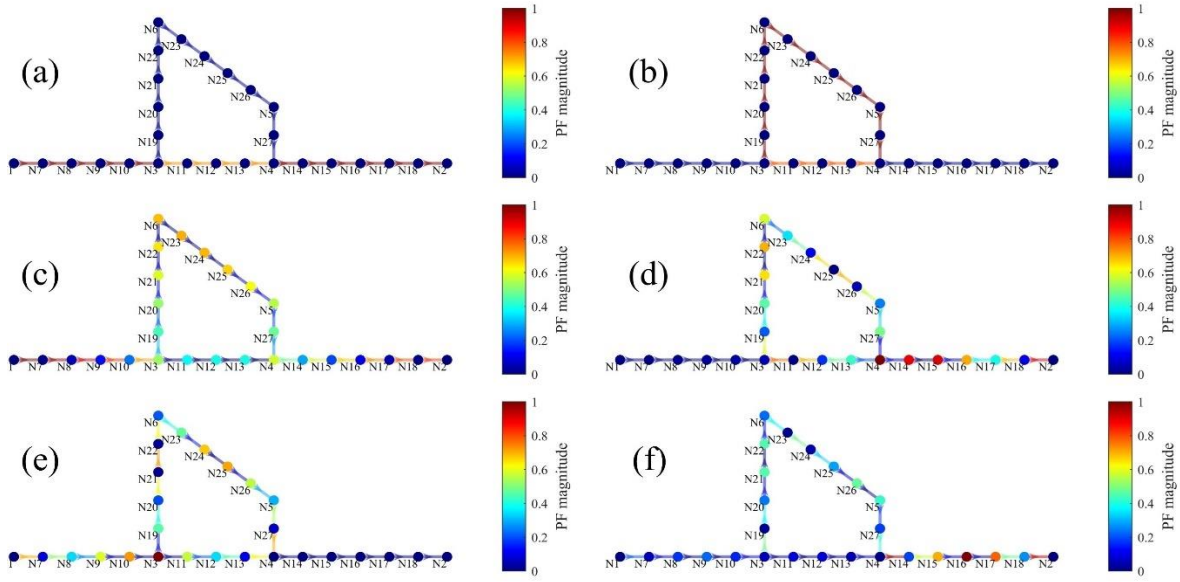


Figure 13. Representation of PF on the network for all valid modes: (a) Mode 1, (b) Mode 2, (c) Mode 3, (d) Mode 4, (e) Mode 5, and (f) Mode 6.

453 For the oscillatory modes, Mode 3 ($-0.032 + 1.263i$), shown in Figure 13 (c), behaves like the
 454 first harmonic of the network. This means there is one anti-node (Node 6) with maximum
 455 potential energy (similar to a mass-spring-damper system) and two nodes with maximum
 456 kinetic energy (Node 1 and 2). Modes 4 ($-0.021 + 3.52i$) and Mode 5 ($-0.019 + 3.71i$) should
 457 be considered together since they form the second harmonic of the system and are closely
 458 related. When both modes are examined simultaneously, it is evident that nodes N3 and N4
 459 serve as anti-nodes for the second harmonic and are the most sensitive locations, experiencing
 460 the most oscillation during the excitation of these modes. For Mode 4, Pipe 1 shows no
 461 participation, while for Mode 5, Pipe 6 shows no participation. For the nodes on the pipe loop,
 462 the participation alternates: if a node has participation in either Mode 4 or 5, it shows little or
 463 no participation in the other. Among them, only Node 23 participates in both modes, with PFs
 464 of 0.38 and 0.47 for modes 4 and 5, respectively.

465 By conducting a time-domain simulation and placing an oscillating demand at Node 23, as in
 466 Test Case 1, the system can be excited. The results of this simulation are shown in Figure 14.
 467 For both frequencies, the system exhibits significant head variation. For excitation with the
 468 frequency of Mode 4 (3.5 rad/s), the maximum head change is 10 meters, while for excitation
 469 with frequency of Mode 5 (3.71 rad/s), the maximum head change is 13.5 meters. These are
 470 considerable head changes for a demand variation of only 0.5 L/s. Although the oscillation
 471 frequencies for these two modes are close, they demonstrate distinct behaviors. From Figure
 472 14, it is evident that node 16 shows no participation in Mode 5 but experiences a 10-meter head
 473 change during oscillation in mode 4.

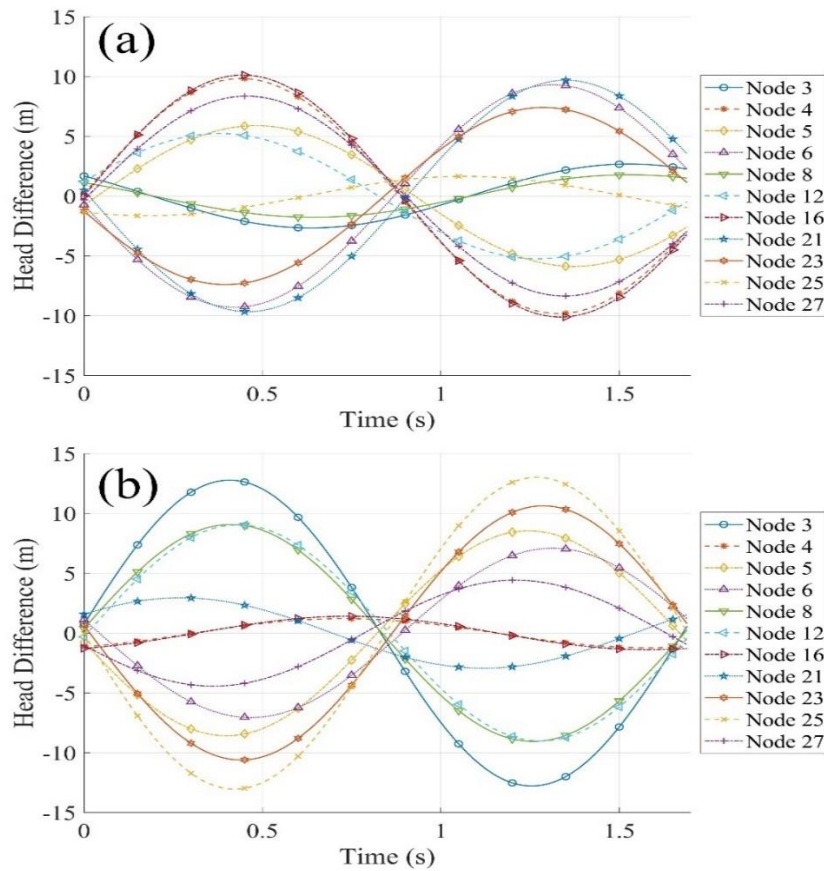


Figure 14. Head change at all internal nodes under steady oscillatory conditions with excitation applied at node 10: (a) oscillation frequency of 3.5 rad/s; (b) oscillation frequency of 3.7 rad/s.

474

475 ***Test case 3: the New York tunnel system***

476 In this test case, the practicality of PF Analysis for WDSs has been investigated. The New York
477 tunnel system has been extensively studied by numerous researchers for both steady-state and
478 transient analysis ([Dandy et al., 1996](#)). One approach to incorporating transient analysis into
479 the design was to identify the worst-case scenario and apply optimization techniques to reduce
480 transient effects ([Jung Bong & Karney Bryan, 2009](#); [Jung et al., 2011](#)).

481 Details of the system can be found in ([Dandy et al., 1996](#)). It was determined that nodes 17 and
482 19, which are dead ends, are more critical compared to other nodes and can generate high
483 transients ([Jung, 2022](#)).

484 In the previous test cases, the system was excited using only a single frequency. However, in
485 real-world scenarios, system excitation consists of a combination of frequencies. Figure 15
486 presents a demand increase over 2 seconds, along with its frequency spectrum. The demand
487 rises from 0 to 0.5 m³/s following a sine-shaped pattern to ensure a gradual transition and avoid
488 introducing artificial high-frequency components. As shown, low frequencies exhibit higher
489 amplitudes compared to high frequencies. This frequency amplitude can be utilized in PF
490 analysis. After identifying the modes, a weighted average of PFs up to the critical frequency
491 can be computed using the frequency amplitude as the weighting factor. Specifically, the
492 amplitudes of each frequency component obtained from the Fourier spectrum (Figure 15 b)
493 were used to weight the normalized participation factors defined in Eq. (26). The weighted
494 average was then calculated as the sum of each mode's PF multiplied by its normalized
495 frequency amplitude, divided by the sum of all amplitudes, ensuring that more strongly excited
496 frequencies contribute proportionally to the overall PF distribution. The resulting averaged PF
497 provides an overall representation of the state contributions to the system's transient response
498 and helps identify critical locations.

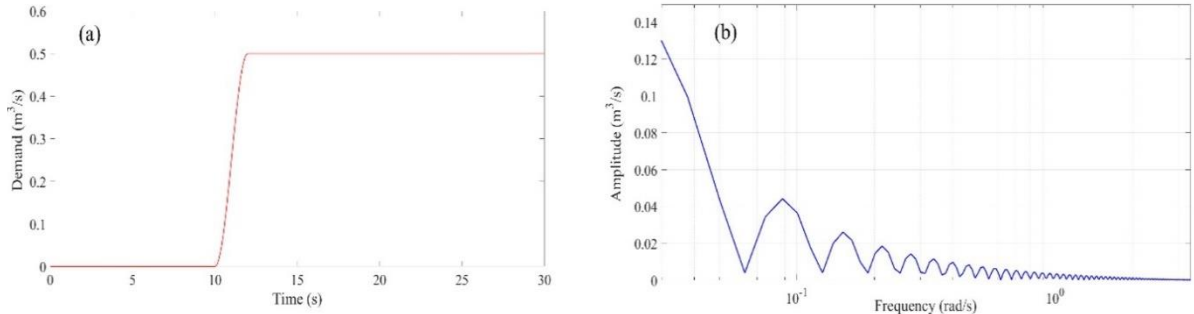


Figure 15. Generated hydraulic transient by increasing demand. The rise follows a sine pattern to smooth the transition: (a) signal in time domain; (b) frequency content of the signal.

499 Figure 16 shows the weighted average PF up to the critical frequency. The system has been
 500 discretized such that a reach is defined every 200 meters. As seen in Figure 16, the dead ends
 501 (nodes 17 and 19) are the most critical nodes. Node N_A , which is also shown in the graph,
 502 exhibits a high PF. This node has not been identified in previous studies. Node 10 also exhibits
 503 a high PF, which can be attributed to a significant impedance mismatch at this location. The
 504 impedance of a pipe is defined as $B = \sqrt{L/C} = a/gS$. An impedance mismatch occurs when
 505 two pipes with different diameters and/or materials (which influence wave speed) are joined
 506 together. Such mismatches are well-known in power systems and fluid dynamics for causing
 507 partial reflection and transmission of transient waves ([Bohorquez et al., 2020](#); [Gong et al., 2013](#);
 508 [Gong et al., 2018](#); [Zeng et al., 2018](#)). In this case, the sudden change in pipe diameter
 509 near Node 10 creates a discontinuity in impedance. When a transient wave generated in a
 510 larger-diameter pipe reaches this node, part of the energy is reflected while the rest is
 511 transmitted with distortion. This interaction excites multiple modes in the system and increases
 512 the dynamic activity at this location, which is why Node 10 appears as a region with high PF
 513 in the analysis. To verify the results, a transient, as shown in Figure 15 has been applied to the
 514 specified nodes, and the system response is presented in Figure 17**Error! Reference source
 515 not found.** The transient behavior of systems with impedance mismatches has been

516 investigated in previous studies, and interested readers are referred to those works for further
517 details ([Bohorquez et al., 2020](#); [Gong et al., 2018](#)).

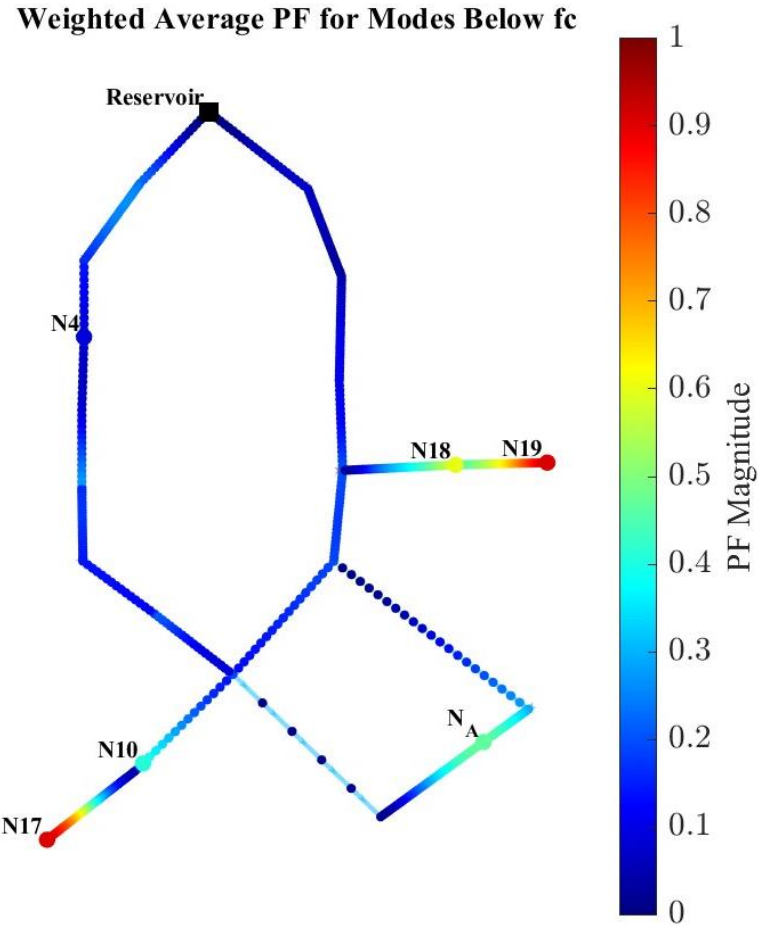


Figure 16. Weighted average PF up to the critical frequency.

518 Figure 17 shows the results of a demand increase at nodes 4, 10, N_A , 17, 18, and 19. Node 4
519 was chosen to demonstrate the system response when the excitation point is a low-PF region.
520 The other nodes, as can be seen, generate high transients in the system according to their PF
521 analysis. By using this approach, intermediate nodes along the pipes can also be investigated,
522 and the accuracy can be increased by increasing the number of discretizations. This approach
523 can provide a clear picture of the vulnerable areas of a WDS to pressure surges and hydraulic
524 transients. The results confirm that exciting the system at nodes 17 and 19 generates high
525 transients.

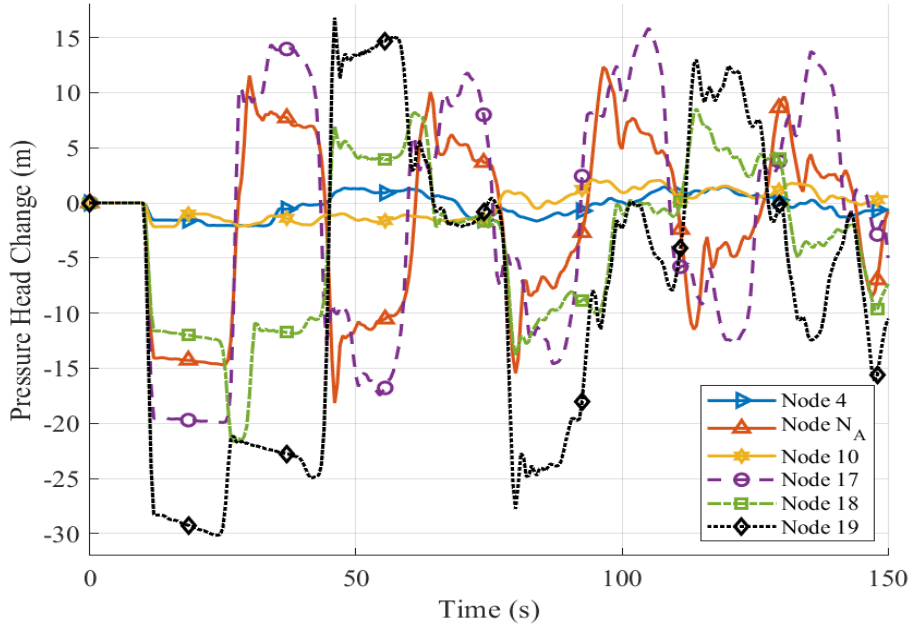


Figure 17. Transient response of the system at excitation points.

526 Practical Considerations, Uncertainties, and Future Directions

527 The numerical examples illustrate that modal analysis can reveal the underlying dynamic
 528 structure of a water distribution system in a way analogous to its use in other engineering
 529 disciplines such as structural or power-system dynamics. As in those fields, the method
 530 provides a means of decomposing complex behaviour into a small number of characteristic
 531 modes, which can assist in understanding and managing system response. However, several
 532 practical considerations and limitations should be acknowledged, as outlined below.

533 First, the framework relies on linearization around a steady operating point. In practice, a
 534 network may operate under multiple demand conditions and flow regimes, each with slightly
 535 different hydraulic behaviour. The analysis can therefore be repeated for several representative
 536 operating points, such as low-, average-, and high-demand scenarios to obtain a family of
 537 modal descriptions. These can be interpreted together to understand how the dominant modes

538 evolve across normal operating conditions. Similarly, the level of spatial discretization
539 determines the highest frequency that can be resolved: finer discretization increases accuracy
540 but also computational cost. The appropriate level depends on the purpose of the study, whether
541 the aim is general behavioural insight, surge assessment, or preparation of reduced-order
542 models for control applications.

543 Second, uncertainties in model parameters such as friction factors, wave speeds, and demand
544 estimates are unavoidable in practice. Experience from related disciplines suggests that such
545 variations shift modal frequencies and damping ratios slightly but rarely change the qualitative
546 pattern of the modes. These uncertainties can be examined through sensitivity analysis or
547 Monte-Carlo sampling to establish confidence intervals for the dominant eigenvalues and to
548 ensure that the identified modes remain physically meaningful. In most cases, the participation-
549 factor distributions are especially robust, because they represent relative spatial contributions
550 rather than absolute magnitudes.

551 Third, applying the method to large networks introduces computational challenges, as the
552 system matrices grow rapidly with the number of pipes and nodes. Nonetheless, the EWCM
553 formulation leads to sparse matrices, where only adjacent elements interact ([Imani et al., 2025](#)).
554 Modern sparse eigensolvers can efficiently extract the few lightly damped modes of
555 engineering interest, making analysis of networks with hundreds of pipes tractable. For very
556 large systems, one practical approach is to focus on critical sub-networks or to use the identified
557 dominant modes to construct reduced-order models that preserve essential dynamics while
558 lowering computational cost.

559 Future work may extend the present framework in several directions. Reduced-order models
560 derived from dominant modes could be coupled with real-time monitoring data to enable faster
561 transient prediction or adaptive control. Incorporating parameter uncertainty directly into the

562 eigen-analysis, for example, through stochastic or interval methods, could further clarify the
563 robustness of modal indicators. Integration with control design and data assimilation
564 frameworks may ultimately allow the method to support operational decision-making, such as
565 identifying excitation sources, refining surge protection strategies, or evaluating the impact of
566 system modifications.

567 **Conclusion**

568 This paper demonstrates the use of the EWCM for modal analysis of water distribution systems
569 WDSs. By linearizing the EWCM around an operating point, a state-space representation is
570 established, allowing the extraction of natural modes through eigenvalue analysis. The results
571 are verified against the AMM in the frequency domain, showing consistent pole locations and
572 damping ratios. The study introduces PF analysis in the time domain to link each mode to its
573 spatial influence within the network. While frequency-domain tools such as the FRD describe
574 resonance behavior, PF analysis reveals how nodal heads and pipe flows contribute to each
575 mode, highlighting locations that are more sensitive to excitation. Time-domain simulations
576 show that inputs applied at high-PF locations generate strong transient responses near the
577 system's fundamental frequency, whereas low-PF excitations lead to minimal response. These
578 results confirm the value of PF analysis for identifying regions where modest disturbances may
579 trigger significant pressure surges due to resonance. The New York tunnel case study
580 demonstrates the practicality of the proposed approach for large-scale networks. Combining
581 modal and PF analyses exposes spatial patterns of vulnerability not evident in frequency
582 analysis alone. From an engineering perspective, PF-based indicators can support resilience
583 assessment by identifying areas more susceptible to transient disturbances, such as sudden

584 demand changes, pump failures, or valve operations. Future work focuses on integrating PF-
585 based monitoring into real-time applications and developing targeted control strategies for
586 transient suppression.

587 Acknowledgements

588 This research is funded by the Australian Research Council through the Discovery Project
589 Grant DP230101513.

590 Data Availability Statement

591 The MATLAB code developed and used in this study to implement the EWCM and perform
592 modal and participation factor analyses of WDSs is publicly available at Zenodo ([Imani, 2025](#)).
593 The code is released under the MIT license and includes the scripts used to reproduce all
594 simulation results and figures in this paper.

595 References

- 596 Abdulrahman, I. (2020). MATLAB-Based Programs for Power System Dynamic Analysis. *IEEE Open Access
597 Journal of Power and Energy*, 7, 59-69. <https://doi.org/10.1109/OAJPE.2019.2954205>
- 598 Abed, E. H., Lindsay, D., & Hashlamoun, W. A. (2000). On participation factors for linear systems. *Automatica*,
599 36(10), 1489-1496. [https://doi.org/https://doi.org/10.1016/S0005-1098\(00\)00082-0](https://doi.org/https://doi.org/10.1016/S0005-1098(00)00082-0)
- 600 Bohorquez, J., Lambert Martin, F., & Simpson Angus, R. (2020). Identifying Head Accumulation due to Transient
601 Wave Superposition in Pipelines. *Journal of Hydraulic Engineering*, 146(1), 04019044.
602 [https://doi.org/10.1061/\(ASCE\)HY.1943-7900.0001631](https://doi.org/10.1061/(ASCE)HY.1943-7900.0001631)
- 603 Che, T.-C., Duan, H.-F., & Lee, P. J. (2021). Transient wave-based methods for anomaly detection in fluid pipes:
604 A review. *Mechanical Systems and Signal Processing*, 160, 107874.
605 <https://doi.org/https://doi.org/10.1016/j.ymssp.2021.107874>
- 606 Dandy, G. C., Simpson, A. R., & Murphy, L. J. (1996). An Improved Genetic Algorithm for Pipe Network
607 Optimization. *Water Resources Research*, 32(2), 449-458.
608 <https://doi.org/https://doi.org/10.1029/95WR02917>

- 609 Dussaud, F. (2015). *An application of modal analysis in electric power systems to study inter-area oscillations*
 610 KTH]. <https://urn.kb.se/resolve?urn=urn:nbn:se:kth:diva-163404>
- 611 Franklin, G., Powell, J., & Emami-Naeini, A. (2010). *Feedback Control of Dynamic Systems*. Prentice-Hall.
- 612 Garofalo, F., Iannelli, L., & Vasca, F. (2002). PARTICIPATION FACTORS AND THEIR CONNECTIONS TO
 613 RESIDUES AND RELATIVE GAIN ARRAY. *IFAC Proceedings Volumes*, 35(1), 125-130.
<https://doi.org/https://doi.org/10.3182/20020721-6-ES-1901.00182>
- 614 Gong, Simpson, A., Lambert, M., Zecchin, A., Kim, Y.-i., & Tijsseling, A. (2013). Detection of Distributed
 615 Deterioration in Single Pipes Using Transient Reflections. *Journal of Pipeline Systems Engineering and*
 616 *Practice*, 4(1), 32-40. [https://doi.org/doi:10.1061/\(ASCE\)PS.1949-1204.0000111](https://doi.org/doi:10.1061/(ASCE)PS.1949-1204.0000111)
- 617 Gong, J., Stephens Mark, L., Lambert Martin, F., Zecchin Aaron, C., & Simpson Angus, R. (2018). Pressure Surge
 618 Suppression Using a Metallic-Plastic-Metallic Pipe Configuration. *Journal of Hydraulic Engineering*,
 619 144(6), 04018025. [https://doi.org/10.1061/\(ASCE\)HY.1943-7900.0001468](https://doi.org/10.1061/(ASCE)HY.1943-7900.0001468)
- 620 He, J., & Fu, Z.-F. (2001). 1 - Overview of modal analysis. In J. He & Z.-F. Fu (Eds.), *Modal Analysis* (pp. 1-11).
 621 Butterworth-Heinemann. <https://doi.org/https://doi.org/10.1016/B978-075065079-3/50001-2>
- 622 Imani, M. (2025). *Morteza2400/ModalAnalysisOfWDSs*: v1.0.0
<https://doi.org/https://doi.org/10.5281/zenodo.15487412>
- 623 Imani, M., Zecchin, A., Zeng, W., & Lambert Martin, F. (2025). Generalization and Analysis of Elastic Water
 624 Column Model for Hydraulic Transient Analysis of Water Distribution Systems. *Journal of Water*
 625 *Resources Planning and Management*, 151(10), 04025054. <https://doi.org/10.1061/JWRMD5.WRENG-6946>
- 626 Jung Bong, S., & Karney Bryan, W. (2009). Systematic Surge Protection for Worst-Case Transient Loadings in
 627 Water Distribution Systems. *Journal of Hydraulic Engineering*, 135(3), 218-223.
[https://doi.org/10.1061/\(ASCE\)0733-9429\(2009\)135:3\(218\)](https://doi.org/10.1061/(ASCE)0733-9429(2009)135:3(218))
- 628 Jung, B. S. (2022). Water Distribution System Optimization Accounting for Worst-Case Transient Loadings.
 629 2022. <https://doi.org/20-29>
- 630 Jung, B. S., Boulos, P. F., & Altman, T. (2011). Optimal transient network design: A multi-objective approach.
 631 *Journal AWWA*, 103(4), 118-127. <https://doi.org/https://doi.org/10.1002/j.1551-8833.2011.tb11440.x>
- 632 Klein, M., Rogers, G. J., & Kundur, P. (1991). A fundamental study of inter-area oscillations in power systems.
 633 *IEEE Transactions on Power Systems*, 6(3), 914-921. <https://doi.org/10.1109/59.119229>
- 634 Lee Pedro, J., Vítkovský John, P., Lambert Martin, F., & Simpson Angus, R. (2008). Valve Design for Extracting
 635 Response Functions from Hydraulic Systems Using Pseudorandom Binary Signals. *Journal of Hydraulic*
 636 *Engineering*, 134(6), 858-864. [https://doi.org/10.1061/\(ASCE\)0733-9429\(2008\)134:6\(858\)](https://doi.org/10.1061/(ASCE)0733-9429(2008)134:6(858))
- 637 Lee, P. J., Lambert, M. F., Simpson, A. R., Vítkovský, J. P., & Liggett, J. (2006). Experimental verification of the
 638 frequency response method for pipeline leak detection. *Journal of Hydraulic Research*, 44(5), 693-707.
<https://doi.org/10.1080/00221686.2006.9521718>
- 639 Lee, P. J., Vítkovský, J. P., Lambert, M. F., Simpson, A. R., & Liggett, J. A. (2005). Frequency Domain Analysis
 640 for Detecting Pipeline Leaks. *Journal of Hydraulic Engineering*, 131(7), 596-604.
[https://doi.org/doi:10.1061/\(ASCE\)0733-9429\(2005\)131:7\(596\)](https://doi.org/doi:10.1061/(ASCE)0733-9429(2005)131:7(596))
- 641 Louati, M., Ghidaoui Mohamed, S., Tekitek Mohamed, M., & Jose Lee, P. (2020). Wave-Leak Interaction in a
 642 Simple Pipe System. *Journal of Hydraulic Engineering*, 146(4), 04020013.
[https://doi.org/10.1061/\(ASCE\)HY.1943-7900.0001714](https://doi.org/10.1061/(ASCE)HY.1943-7900.0001714)
- 643 Shimada, M. (1992). State-Space Analysis and Control of Slow Transients in Pipes. *Journal of Hydraulic*
 644 *Engineering*, 118(9), 1287-1304. [https://doi.org/10.1061/\(ASCE\)0733-9429\(1992\)118:9\(1287\)](https://doi.org/10.1061/(ASCE)0733-9429(1992)118:9(1287))
- 645 Souza, O. H., Barbieri, N., & Santos, A. H. M. (1999). Study of hydraulic transients in hydropower plants through
 646 simulation of nonlinear model of penstock and hydraulic turbine model. *IEEE Transactions on Power*
 647 *Systems*, 14(4), 1269-1272. <https://doi.org/10.1109/59.801883>
- 648 Ulanicki, B., & Beaujean, P. (2021). Modeling Dynamic Behavior of Water Distribution Systems for Control
 649 Purposes. *Journal of Water Resources Planning and Management*, 147(8), 04021043.
[https://doi.org/10.1061/\(ASCE\)WR.1943-5452.0001403](https://doi.org/10.1061/(ASCE)WR.1943-5452.0001403)
- 650 Wylie, E. B., and V. L. Streeter. (1993). *Fluid transients in systems*. Prentice Hall.
- 651 Xing, L., & Sela, L. (2020). Transient simulations in water distribution networks: TSNet python package.
 652 *Advances in Engineering Software*, 149, 102884.
<https://doi.org/https://doi.org/10.1016/j.advengsoft.2020.102884>
- 653 Zecchin, A., Kim, S., & Ferrante, M. (2018). *A modal-based analysis of pipeline networks with applications to*
 654 *time-domain simulation* 13th International Conference on Pressure Surges,
- 655 Zecchin, A. C. (2010). *Laplace-domain analysis of fluid line networks with applications to time-domain*
 656 *simulation and system parameter identification* Ph.D. thesis, School of Civil, Environmental & Mining
 657 Engineering, Univ. of Adelaide].

- 667 Zecchin, A. C., Simpson, A. R., Lambert, M. F., White, L. B., & Vítkovský, J. P. (2009). Transient Modeling of
 668 Arbitrary Pipe Networks by a Laplace-Domain Admittance Matrix. *Journal of Engineering Mechanics*,
 669 135(6), 538-547. [https://doi.org/doi:10.1061/\(ASCE\)0733-9399\(2009\)135:6\(538\)](https://doi.org/doi:10.1061/(ASCE)0733-9399(2009)135:6(538))
- 670 Zeng, W., Gong, J., Zecchin Aaron, C., Lambert Martin, F., Simpson Angus, R., & Cazzolato Benjamin, S. (2018).
 671 Condition Assessment of Water Pipelines Using a Modified Layer-Peeling Method. *Journal of Hydraulic
 672 Engineering*, 144(12), 04018076. [https://doi.org/10.1061/\(ASCE\)HY.1943-7900.0001547](https://doi.org/10.1061/(ASCE)HY.1943-7900.0001547)
- 673 Zeng, W., Zecchin Aaron, C., & Lambert Martin, F. (2022). Elastic Water Column Model for Hydraulic Transient
 674 Analysis of Pipe Networks. *Journal of Hydraulic Engineering*, 148(12), 04022027.
 675 [https://doi.org/10.1061/\(ASCE\)HY.1943-7900.0002028](https://doi.org/10.1061/(ASCE)HY.1943-7900.0002028)

676

677 Appendix: RWCM Eigen Analysis

678 In the RWCM, fewer state variables are used compared to the EWCM. Specifically, in the
 679 RWCM, the state variables are limited to independent flow variables. This reduction in the
 680 number of state variables presents challenges when deriving the Jacobian matrix from the
 681 momentum equation, as the interconnection between the variables complicates the process. The
 682 RWCM assumes an infinite wave speed, a key assumption that simplifies the fundamental
 683 governing equations, which are expressed as follows ([Shimada, 1992](#)):

$$\mathbf{L} \frac{d\mathbf{q}}{dt} = -\mathbf{R} \text{diag}\{|\mathbf{q}|\} \mathbf{q} + \mathbf{A}_I^T \mathbf{h}_I + \mathbf{A}_R^T \mathbf{h}_R \quad (35)$$

$$\mathbf{A}_I \mathbf{q} = -\mathbf{Q}_I \quad (36)$$

684 The derivation starts by differentiating Eq. (36) and substituting Eq. (35), leading to an
 685 expression for the internal heads \mathbf{h}_I :

$$\mathbf{h}_I = \mathbf{K}^{-1} \left(\mathbf{A}_I \mathbf{L}^{-1} [\mathbf{R} \text{diag}\{|\mathbf{q}|\} \mathbf{q} - \mathbf{A}_R^T \mathbf{h}_R] - \frac{\mathbf{Q}_I(t)}{dt} \right) \quad (37)$$

686 Here, $\mathbf{K} = \mathbf{A}_I \mathbf{L}^{-1} \mathbf{A}_I^T$ and, when \mathbf{h}_I is substituted back into Eq. (35), the following expression is
 687 derived:

$$\begin{aligned} \frac{\partial \mathbf{q}}{\partial t} = & \mathbf{L}^{-1}\{-\mathbf{A}_I^T \mathbf{K}^{-1} \mathbf{A}_I \mathbf{L}^{-1} - \mathbf{I}\} \mathbf{R} \text{diag}\{|\mathbf{q}|\} \mathbf{q} - \mathbf{L}^{-1} \mathbf{A}_I^T \mathbf{K}^{-1} \frac{\mathbf{Q}_I(t)}{dt} \\ & + \mathbf{L}^{-1}\{\mathbf{A}_R^T \mathbf{h}_R - \mathbf{A}_I^T \mathbf{K}^{-1} \mathbf{A}_I \mathbf{L}^{-1} \mathbf{A}_R^T \mathbf{h}_R\} \end{aligned} \quad (38)$$

688 Defining $\mathbf{W} = \mathbf{L}^{-1}(\mathbf{I} - \mathbf{A}_I^T \mathbf{K}^{-1} \mathbf{A}_I \mathbf{L}^{-1})$, and incorporating the permutation matrix \mathbf{P} , which
 689 organizes the state variables into independent and dependent flows, leads to the refined
 690 equation:

$$\mathbf{P} \frac{d\mathbf{q}}{dt} = -\mathbf{P} \mathbf{W} \mathbf{P}^{-1} \mathbf{P} [\mathbf{R} \text{diag}\{|\mathbf{q}|\} \mathbf{q} - \mathbf{A}_R^T \mathbf{h}_R] + \mathbf{P} \mathbf{L}^{-1} \mathbf{A}_I^T \mathbf{K}^{-1} \frac{d\mathbf{Q}_I}{dt} \quad (39)$$

691 The first n_i rows of this equation set form a set of ODEs for RWCM, allowing the
 692 determination of \mathbf{q}_i , the independent flow rates. Eq. (40) simplifies the matrix expression,
 693 while Eq. (41) provides the dynamics of \mathbf{q}_i :

$$\mathbf{P} \mathbf{W} \mathbf{P}^{-1} = \begin{pmatrix} \mathbf{W}_i \\ \mathbf{W}_d \end{pmatrix} \quad (40)$$

$$\frac{d\mathbf{q}_i}{dt} = -\mathbf{W}_i \mathbf{P} [\mathbf{R} \text{diag}\{|\mathbf{q}|\} \mathbf{q} - \mathbf{A}_R^T \mathbf{h}_R] + \mathbf{P} \mathbf{L}^{-1} \mathbf{A}_I^T \mathbf{R}^{-1} \frac{d\mathbf{Q}_I}{dt} \quad (41)$$

694 Alternatively, the flow vector \mathbf{q} is partitioned into \mathbf{q}_i (independent flow rates) and \mathbf{q}_d
 695 (dependent flow rates), where \mathbf{q}_d is expressed as a function of \mathbf{q}_i , following Shimida (1992):

$$\mathbf{q}_d = -\mathbf{A}_{Id}^{-1} (\mathbf{A}_{ii} \mathbf{q}_i + \mathbf{Q}_I) \quad (42)$$

696 Two additional matrices, \mathbf{E}_{i1}^T and \mathbf{E}_{i2}^T , are introduced to decompose \mathbf{W}_i as follows:

$$\mathbf{E}_{i1}^T = [\mathbf{I}_{n_i} \ \mathbf{0}_{n_i \times n_D}] \quad (43)$$

$$\mathbf{E}_{i2}^T = [\mathbf{0}_{n_D \times n_i} \ \mathbf{I}_{n_D}] \quad (44)$$

697 Here, n_D represents the number of dependent pipes, and n_i represents the number of
 698 independent pipes. By applying Eqs. (43) and (44) to the first term on the right-hand side of
 699 Eq. (41) the following relationship is established:

$$\mathbf{W}_i \mathbf{P}[-\mathbf{R}\text{diag}\{|\mathbf{q}|\}\mathbf{q}] = -\mathbf{W}_{i1} \mathbf{R}\text{diag}\{\mathbf{q}_i\}\mathbf{q}_i - \mathbf{W}_{i1} \mathbf{R}\text{diag}\{\mathbf{q}_d\}\mathbf{q}_d \quad (45)$$

$$\mathbf{W}_{i1} = \mathbf{W}_i \mathbf{E}_{i1}^T \quad (46)$$

$$\mathbf{W}_{i2} = \mathbf{W}_i \mathbf{E}_{i2}^T$$

700 Eq. (42) is substituted into Eq. (41), resulting in:

$$\mathbf{W}_i \mathbf{P}[-\mathbf{R}\text{diag}\{|\mathbf{q}|\}\mathbf{q}] = -\mathbf{W}_{i1} \mathbf{R}\text{diag}\{\mathbf{q}_i\}\mathbf{q}_i - \mathbf{W}_{i2} \mathbf{R}\text{diag}\{\mathbf{q}_d\}(-\mathbf{A}_{Id}^{-1}(\mathbf{A}_{Ii}\mathbf{q}_i + \mathbf{Q}_I)) \quad (47)$$

701 Substituting Eq. (47) into Eq. (41) and taking the derivative, the Jacobian matrix is derived as
 702 follows:

$$\mathbf{J} = -2\mathbf{W}_{i1} \mathbf{R}_i \text{diag}\{|\mathbf{q}_i|\} - 2\mathbf{W}_{i2} \text{diag}\{\mathbf{R}_d|-\mathbf{A}_{Id}^{-1}(\mathbf{A}_{Ii}\mathbf{q}_i + \mathbf{Q}_I)|\}(-\mathbf{A}_{Id}^{-1}(\mathbf{A}_{Ii})) \quad (48)$$

703 The eigenvalues of the Jacobian matrix are real and negative, corresponding to the damped
 704 modes of the system. These eigenvalues represent the decay rates of the system's dynamic
 705 response, showing how quickly transient events are damped in the RWCM.